

$^{13}\text{CO}(1-0)$ and $^{12}\text{CO}(2-1)$ in the center of the barred galaxy NGC 1530

D. Reynaud^{1,2} and D. Downes¹

¹ Institut de Radio Astronomie Millimétrique, F-38406 Saint Martin d'Hères, France

² CEA/DSM/DAPNIA/SAP, C.E. Saclay, F-91191 Gif-sur-Yvette Cedex, France

Received date; accepted date

Abstract. We present $^{13}\text{CO}(1-0)$ and $^{12}\text{CO}(2-1)$ aperture synthesis maps of the barred spiral galaxy NGC 1530. The angular resolutions are respectively $3''.1$ and $1''.6$. Both transitions show features similar to the $^{12}\text{CO}(1-0)$ map, with a nuclear feature (a ring or unresolved spiral arms) surrounded by two curved arcs. The average line ratios are $^{12}\text{CO}(1-0)/^{13}\text{CO}(1-0) = 9.3$ and $^{12}\text{CO}(2-1)/^{12}\text{CO}(1-0) = 0.7$. The $^{12}\text{CO}/^{13}\text{CO}$ ratio is lower in the circumnuclear ring (6–8) than in the arcs (11–15). We fit the observed line ratios by escape probability models, and deduce that the gas density is probably higher in the nuclear feature ($\geq 5 \times 10^2 \text{ cm}^{-3}$) than in the arcs ($\simeq 2 \times 10^2 \text{ cm}^{-3}$), confirming earlier HCN results. The kinetic temperatures are in the range 20–90 K, but are weakly constrained by the model. The average filling factor of the $^{12}\text{CO}(1-0)$ emitting gas is low, $\simeq 0.15$. The cm-radio continuum emission also peaks in the nuclear feature, indicating a higher rate of star formation than in the arcs. We derive values for the CO luminosity to molecular gas mass conversion factor between 0.3 and $2.3 M_{\odot} (\text{K km s}^{-1} \text{ pc}^2)^{-1}$, significantly lower than the standard Galactic value.

Key words: galaxies: structure – galaxies: individual (NGC 1530) – galaxies: ISM – galaxies: kinematics and dynamics – radio lines: galaxies

1. Introduction

Except for the $^{12}\text{CO}(1-0)$ line, few detailed maps of the molecular gas distribution in galaxies have been published so far. $^{13}\text{CO}(1-0)$ has been rarely observed in galaxies, and $^{12}\text{CO}(2-1)$ even more rarely. The weakness of the $^{13}\text{CO}(1-0)$ line in galaxies and the technical problems of observing at the 230 GHz frequency of $^{12}\text{CO}(2-1)$ account for this rarity of observations. However, for a better knowledge of the interstellar medium in galaxies, more tracers than $^{12}\text{CO}(1-0)$ must be observed. A

crucial issue that can be studied through these observations is the validity of the conversion factor $M(\text{H}_2)/L_{\text{CO}} \simeq 4.8 M_{\odot} (\text{K km s}^{-1} \text{ pc}^2)^{-1}$ that is valid for self-gravitating molecular clouds (see Sage & Isbell 1991).

$^{13}\text{CO}(1-0)$ has been observed with interferometers in only a few galaxies. In IC 342, a galaxy similar to the Milky Way, Wright et al. (1993) showed a variation of the intensity ratio $R_{12/13} = ^{12}\text{CO}(1-0)/^{13}\text{CO}(1-0)$. Those authors interpret ^{13}CO peaks as molecular clouds while ^{12}CO would trace a more diffuse medium. The variations of $R_{12/13}$ can be interpreted in different ways (Sage & Isbell 1991, Sakamoto et al. 1997), including variation of gas density, kinetic temperature, and relative abundance of isotopes. Downes et al. (1992) explained these ratio variations by filling factors of clouds varying across the central part of IC 342.

Up to now $^{12}\text{CO}(2-1)$ has been observed mainly in the GMCs of our Galaxy, where the ratio $R_{21/10} = ^{12}\text{CO}(2-1)/^{12}\text{CO}(1-0)$ has a typical value of 1.0 (Plambeck & Williams 1979), indicating gas at low kinetic temperature (~ 10 K). Radford et al. (1991) observed a low ratio $R_{21/10} \simeq 0.6 - 0.75$ in infrared-luminous galaxies, indicating the presence of subthermally excited CO. Braine et al. (1993) surveyed of 81 galaxies in the CO transitions, and found a average ratio $R_{21/10} \simeq 0.89$, indicating cold, optically thick gas. Similarly in the central region of IC 342, Eckart et al. (1990) found a ratio $R_{21/10} \approx 1.0$ everywhere, with a slightly higher value in the center, possibly indicating an increase in the gas kinetic temperature toward the center. A ratio $R_{21/10} \approx 1.4$ was found close to a CO arm, indicating warm gas heated by star formation. The starburst galaxy M82 shows a different behaviour, with an unusually high ratio $R_{21/10} \approx 2.5$ (Knapp et al. 1980, Loiseau et al. 1990), indicating hot gas (> 40 K) heated by star formation.

We have observed in the $^{13}\text{CO}(1-0)$ and $^{12}\text{CO}(1-0)$ lines the central region ($\simeq 5$ kpc) of the barred spiral galaxy NGC 1530. This galaxy contains large amount of molecular gas in its central kiloparsec, due to the accreting action of its bar (cf models by Athanassoula 1992, Friedli & Benz 1993, Piner, Stone, & Teuben 1995). The

Table 1. IRAM interferometer parameters.

| Parameter | $^{13}\text{CO}(1-0)$ | $^{12}\text{CO}(2-1)$ |
|--|-----------------------|-----------------------|
| Frequency (GHz) | 109.3 | 228.7 |
| Calibrator flux (Jy) ^a | 1.1 | 0.5 |
| Beam (FWHM) | $3''.4 \times 2''.9$ | $1''.8 \times 1''.4$ |
| Beam (p.a.) | -76° | -122° |
| T_b/S (K/Jy) | 10.4 | 9.0 |
| r.m.s. noise (mJy beam^{-1}) ^b | 1.5 | 5.0 |

^a Source=0224+671^b Noise in 20 km s^{-1} channels

bar has driven a high fraction ($\simeq 25\%$) of the total gas of the galaxy into the center (Downes et al. 1996, DRSR hereafter). CO(1–0) has been extensively studied in this galaxy (Regan et al. 1995, DRSR, Reynaud & Downes 1997 (RD 97), Reynaud & Downes 1998). RD 97 also mapped HCN(1–0), showing that the dense gas as traced by HCN is mainly concentrated in a nuclear ring or unresolved spiral at galactic radius $\leq 1 \text{ kpc}$. This concentration of dense gas is connected with the presence of an inner Lindblad resonance at radius $\simeq 1.2 \text{ kpc}$.

The ionized gas was mapped in H α by Regan et al. (1996). Greve et al. (1999) compared the distribution and kinematics of ionized and molecular gas in the bar of NGC 1530.

2. Observations, Data reduction

The observations were made with the IRAM interferometer on Plateau de Bure, France, with four 15m antennas (Guilloteau et al. 1992) between November 1995 and April 1996. Each antenna of the interferometer was equipped with a dual channel receiver tuned to frequencies 109.3 GHz and 228.7 GHz, corresponding to $^{13}\text{CO}(1-0)$ and $^{12}\text{CO}(2-1)$. The tracking center of the interferometer was $04^{\text{h}}23^{\text{m}}27^{\text{s}}.32$, $+75^\circ17'45''.0$ (J2000), close to the nucleus of the galaxy. The recession velocity of the galaxy is $\simeq 2470 \text{ km s}^{-1}$. See DRSR for a table with the astrophysical parameters of the galaxy.

The interferometer was used in 3 configurations, giving baselines between 20m and 180m. After Fourier transform of the visibilities and restoration by the CLEAN algorithm, we obtained channel maps of both transitions with a 20 km s^{-1} velocity width. The observational parameters are summarised in Table 1, including the clean beam parameters and the final noise in channel maps.

3. Observational Results

3.1. Molecular maps

Figure 1 shows the integrated $^{13}\text{CO}(1-0)$ and $^{12}\text{CO}(2-1)$ of the inner $30''$ of NGC 1530. In the same figure are also displayed for comparison the integrated $^{12}\text{CO}(1-0)$ and HCN(1–0) maps from RD 97. The integration ranges are respectively 540 km s^{-1} ($^{12}\text{CO}(1-$

$0)$, 520 km s^{-1} ($^{12}\text{CO}(2-1)$), 360 km s^{-1} ($^{13}\text{CO}(1-0)$), and 180 km s^{-1} (HCN(1–0)). Each map is corrected for the primary beam attenuation. The primary beams (FWHM) are respectively $43''$ ($^{12}\text{CO}(1-0)$), $21''$ ($^{12}\text{CO}(2-1)$), $45''$ ($^{13}\text{CO}(1-0)$), and $56''$ (HCN(1–0)). These maps are centered on the dynamical center of the galaxy, which has coordinates $04^{\text{h}}23^{\text{m}}26^{\text{s}}.7$, $75^\circ17'44''.0$ (J2000) (from RD 97), i.e. $2.5''$ from the tracking center of the interferometer.

The $^{12}\text{CO}(2-1)$ map is truncated beyond a diameter of $42''$. Structures visible at the truncation limit are probably real molecular clouds deformed by the high noise level, since the noise is amplified by the primary beam correction. The two transitions of ^{12}CO give similar maps, with two arcs, and inside them, a central structure which is a ring or unresolved nuclear spiral arms. These two maps have similar resolutions, $1''.8$ and $1''.6$ for $^{12}\text{CO}(1-0)$ and $^{12}\text{CO}(2-1)$ respectively. The $^{13}\text{CO}(1-0)$ map is grossly similar to the ^{12}CO maps, with a beam twice as large ($3''.1$). However the arcs seem dimmer in ^{13}CO than in ^{12}CO . There is a real difference between the brightness of the arcs and the brightness of the nuclear feature, a difference which had already been detected in HCN (see Fig. 1 and Fig. 3 of RD 97). The difference is confirmed on the ratio map obtained by smoothing $^{12}\text{CO}(1-0)$ to the resolution of $^{13}\text{CO}(1-0)$ (Fig. 5).

Figure 2 shows the 20 km s^{-1} channel maps of the $^{13}\text{CO}(1-0)$ emission. Figure 3 shows the channel maps of the $^{12}\text{CO}(2-1)$ emission. These maps are not corrected for the primary beam attenuation. The kinematic pattern shown by these maps is the same as that found by RD 97 in the $^{12}\text{CO}(1-0)$ transition. That is, the kinematics of the gas in the arcs shows large (100 km s^{-1}) infall motions (due to the x_1 orbits along the bar) and in the central feature shows mainly circular rotation or weakly elliptical orbits (the x_2 orbits normal to the bar). Figure 4 shows position-velocity diagrams in the CO(2–1) (left panel) and the CO(1–0) (right panel) transitions. These diagrams are cuts in the data cube, along the line of nodes passing through the dynamical center. The circular component is therefore the only component of the velocity field detected on these diagrams. The maximal radius of the emission is 1.4 kpc . The diagrams are very similar in the two transitions of CO, with a steep rising part in the central $3''$ region and a flattening of the rotation curve at the crossing of the nuclear feature (incomplete ring or spiral within a $6''$ diameter of the nucleus). Outside this region, the rotation curve is steep (see Fig. 4 at radii of $8''$).

3.2. Line ratios

For a quantitative analysis of the previous maps, we made maps of the ratios of the various integrated intensities, corrected for their respective primary beams. This correction makes the noise non-uniform through the ratio maps, especially in the $^{12}\text{CO}(2-1)$ transition. Figures 5 and 6 show the ratios $^{12}\text{CO}(1-0)/^{13}\text{CO}(1-0)$ and $^{12}\text{CO}(2-1)/^{12}\text{CO}(1-$

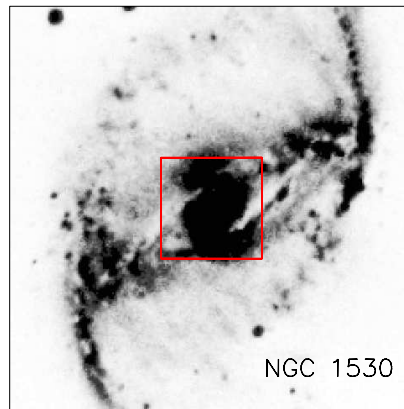
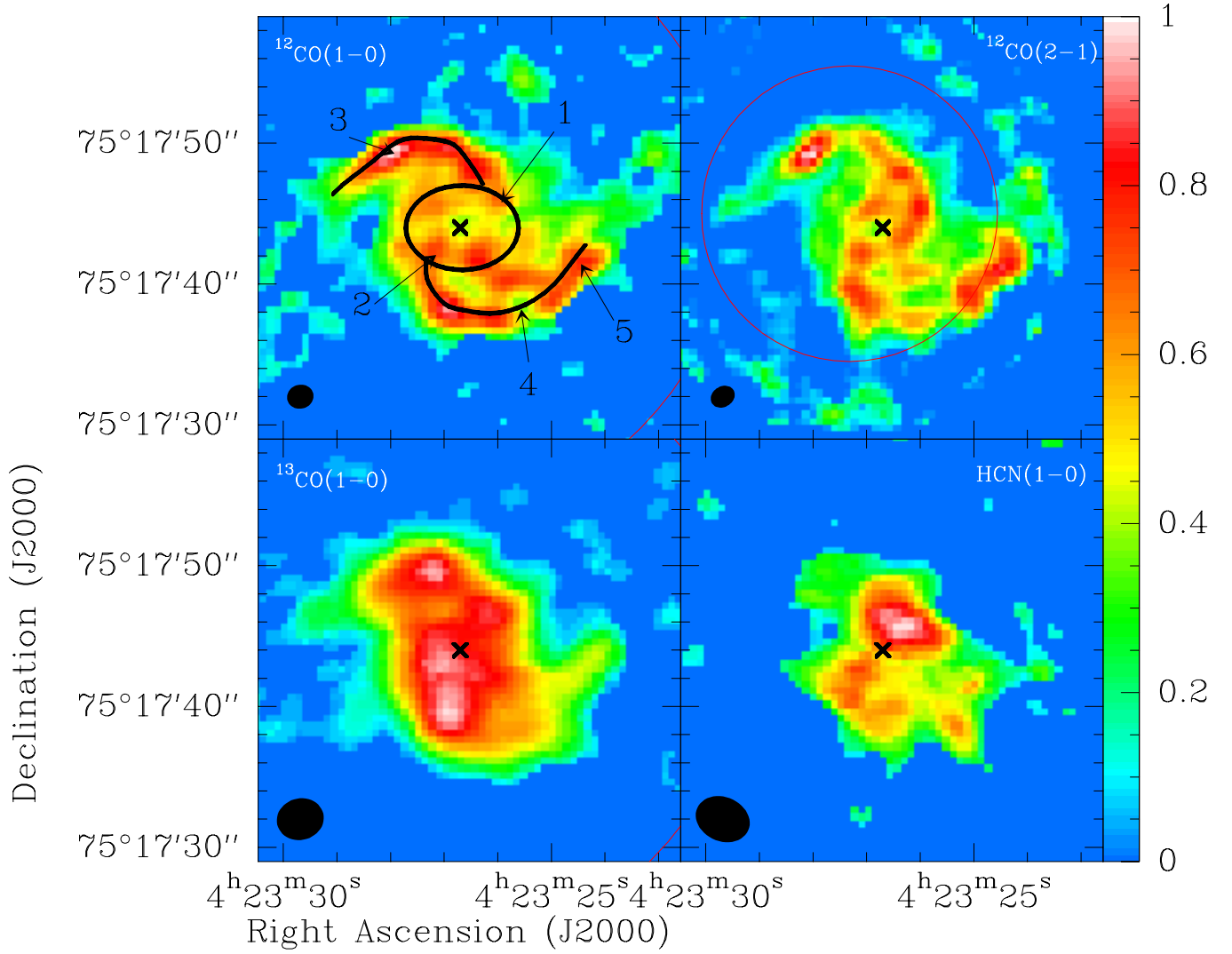


Fig. 1. False color maps of four velocity integrated transitions. *a*) upper left: $^{12}\text{CO}(1-0)$. Labels indicate the regions described in section 4.1. A sketch of the arcs and the nuclear feature (ring or unresolved spiral arms displayed as an ellipse) is also displayed (full black line). *b*) upper right: $^{12}\text{CO}(2-1)$. *c*) lower left: $^{13}\text{CO}(1-0)$. *d*) lower right: $\text{HCN}(1-0)$. For each map the **X** sign indicates the position of the dynamical center, and the clean beam is indicated at lower left. Each map is corrected for the primary beam attenuation (see text). The primary beams (FWHM) are shown as red circles. The color scale is indicated at the right of the diagram. The minimum displayed flux are 0 for all transitions, except for $^{12}\text{CO}(2-1)$ where it is $3 \text{ Jy beam}^{-1} \text{ km s}^{-1}$. The maxima correspond to the value 1 on the color scale, and are $10.0 \text{ Jy beam}^{-1} \text{ km s}^{-1}$ ($^{12}\text{CO}(1-0)$), 25.0 ($^{12}\text{CO}(2-1)$), 2.7 ($^{13}\text{CO}(1-0)$) and 1.7 ($\text{HCN}(1-0)$) respectively. The bottom panel shows an optical image of the bar and a part of the spiral arms of NGC 1530 (Optical image NOAO). The red

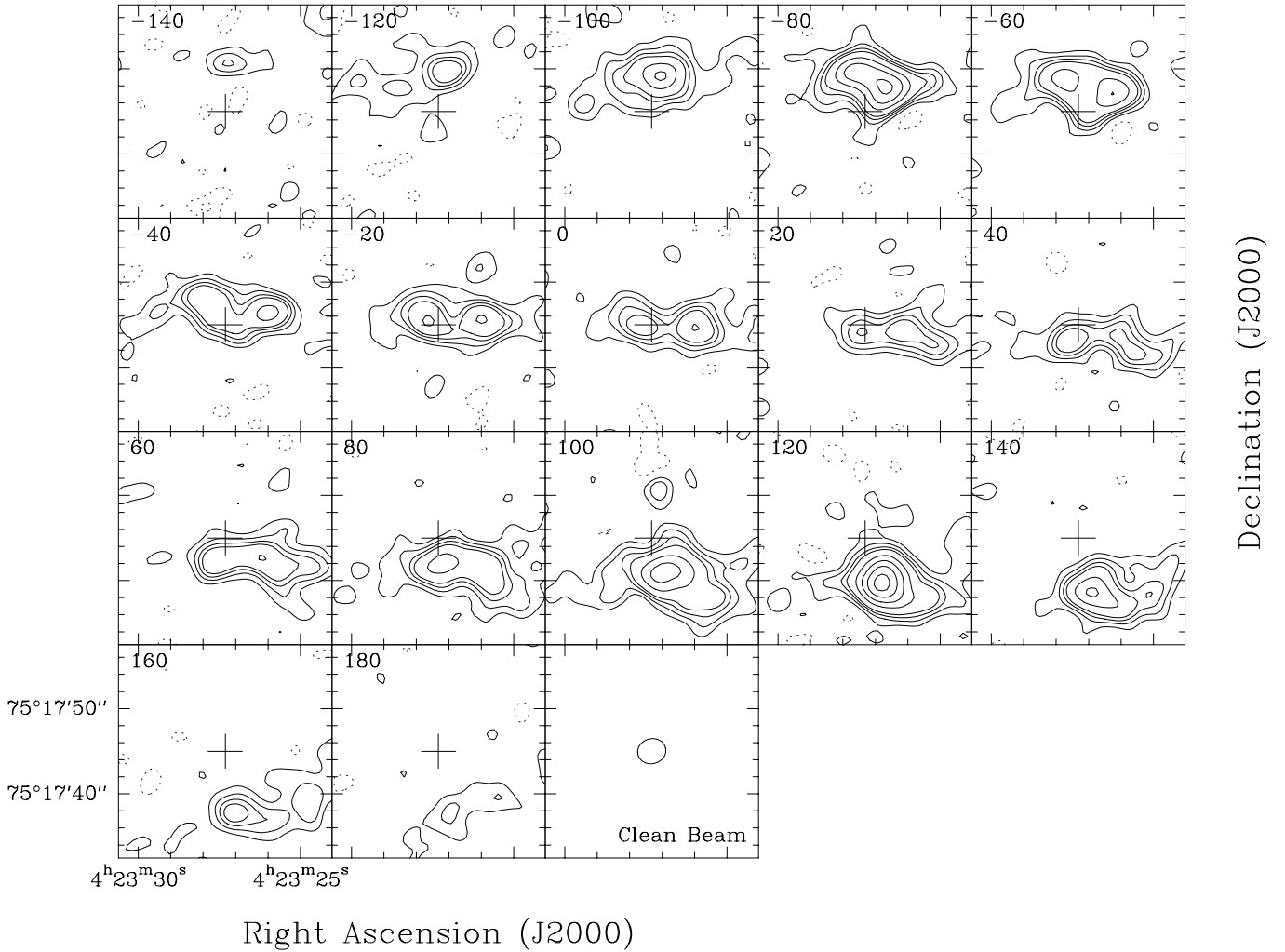


Fig. 2. $^{13}\text{CO}(1-0)$ maps of the central $25''$ of NGC 1530 in 20 km s^{-1} wide channels. Radial velocities (km s^{-1} , upper left of each box) are relative to 2450 km s^{-1} . The contour intervals are $-6, -3, 3, 6, 9, 12, 21, 30, 39, 48 \text{ mJy beam}^{-1}$ ($\sigma = 1.5 \text{ mJy beam}^{-1}$). The cross indicates the position of the tracking center of the interferometer ($\alpha = 4^{\text{h}}23^{\text{m}}27^{\text{s}}.3$, $\delta = 75^{\circ}17'45''.0$; J2000). The $3''.4 \times 2''.9$ clean beam is shown in the lower right box.

0) respectively. Each ratio map was made by smoothing the map with the higher resolution to that of the lower-resolution map.

Ratio map $R_{12/13} = ^{12}\text{CO}(1-0)/^{13}\text{CO}(1-0)$: The resolution is $\approx 3''.1$. $^{13}\text{CO}(1-0)$ is detected in the same places as $^{12}\text{CO}(1-0)$, so the ratio can be studied in the entire CO nuclear disk. The average value is $\langle R_{12/13} \rangle \approx 9.5 \pm 3.5$. The ratio is about 6 to 8 in the central zone (inside the two CO arcs), with the lowest value ($R \approx 6$) near the center of NGC 1530. The value is 11 to 15 in the arcs, with a maximum value of 15. The spatial distribution of dense gas ($n \approx 10^4 \text{ cm}^{-3}$) is best shown in the HCN map (see Fig. 1). The ratio CO/HCN is 7 to 10 in the central ring of NGC 1530 (between the two arcs), while in the arcs this ratio is larger, in the range 14 to 30. The $^{12}\text{CO}(1-0)/^{13}\text{CO}(1-0)$ ratio thus seems to have the same characteristics as the CO/HCN ratio.

Ratio map $R_{21/10} = ^{12}\text{CO}(2-1)/^{12}\text{CO}(1-0)$: The resolution is $\approx 1''.8$. The ratio can be studied in the entire disk with a high signal-to-noise ratio. The average ratio is $\langle R_{21/10} \rangle \approx 0.7 \pm 0.2$. The ratio is ≈ 1.0 over a large region $4'' \times 2''$ wide, with the dynamical center of the galaxy on the eastern edge of this region (see Fig. 6). The maximum value is 1.2, at a position $3''$ west of the dynamical center. Between the two arcs, the ratio is generally > 0.7 . In the northern arc, the ratio is 0.4 to 0.7 while in the southern arc it is 0.5 to 1.1.

3.3. Radio continuum maps

NGC 1530 was observed with the Very Large Array¹ (VLA) in a snapshot mode. Saikia et al. (1994) show

¹ The VLA is a facility of the National Radio Astronomy Observatory.

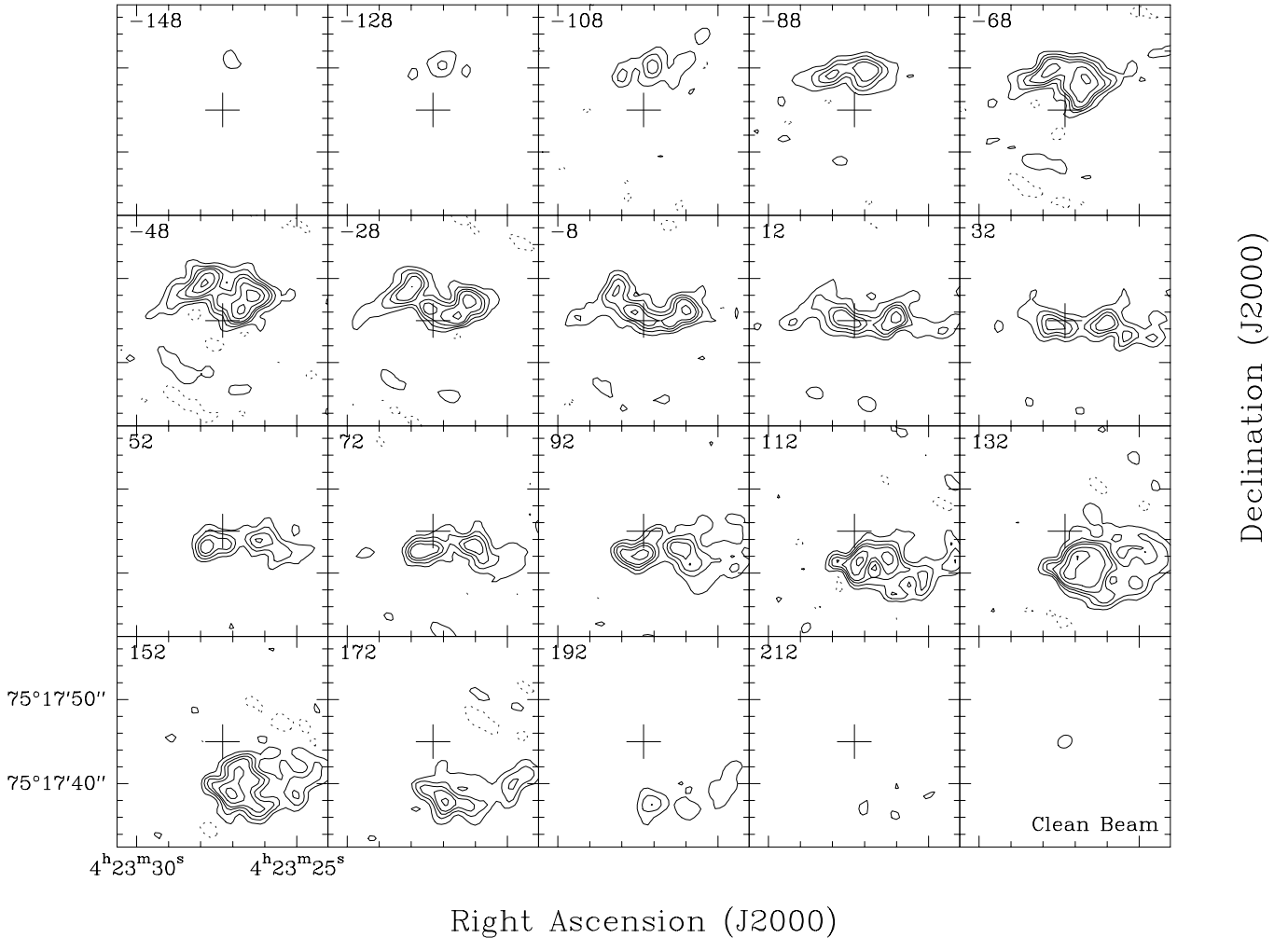


Fig. 3. $^{12}\text{CO}(2-1)$ maps of the central $25''$ of NGC 1530 in 20 km s^{-1} wide channels. Radial velocities (km s^{-1} , upper left of each box) are relative to 2429 km s^{-1} . The contour intervals are $-60, -30, 30, 60, 90, 120, 180, 240, 300 \text{ mJy beam}^{-1}$ ($\sigma = 5 \text{ mJy beam}^{-1}$). The cross indicates the position of the phase tracking center of the interferometer. The $1''.8 \times 1''.4$ clean beam is shown in the lower right box.

the 20 cm emission map made with uniform weighting. Figure 7 shows the same data, at 20 and 6 cm, in maps obtained with natural weighting, which allows maximum sensitivity. Superposed on the cm maps are a few contours of the $^{12}\text{CO}(2-1)$ distribution. The beam sizes are $1''.6 \times 1''.5$ (p.a. -35°) at 20 cm and $1''.6 \times 1''.3$ (p.a. -32°) at 6 cm, both similar to the beam at $\text{CO}(2-1)$. The emission peaks are 11σ at 20 cm and 8σ at 6 cm, so the detected features are not prominent in the maps. The 20 cm distribution has two types of emission: a weak (3σ) emission over most of the molecular disk, and a number of compact components, unresolved by the interferometer. These components are mainly distributed along a ring, around a central cavity. The radius of this ring is about $3''$, i.e. 500 pc. This ring coincides with the one obtained in the $^{12}\text{CO}(2-1)$ and $^{12}\text{CO}(1-0)$ lines. A strong component is detected $5''$ south of the dynamical center. It coincides well with a CO compact component. The 6 cm map shows

with a lower signal-to-noise ratio the same distribution as the 20 cm map, i.e. a strong ring distribution.

For the central $30''$ of NGC 1530, integrated fluxes are 30 mJy at 20 cm and 8.6 mJy at 6 cm (integration threshold: 3σ). The galaxy emits a total of 80 mJy at 20 cm and 37 mJy at 6 cm (Wunderlich et al. 1987, Condon et al. 1996). Thus 37% and 23% are emitted in the central $30''$ (i.e. 5 kpc along the major axis) of NGC 1530. The 500 pc ring shares about 50% of the central centimeter continuum emission, which is more than the $^{12}\text{CO}(1-0)$ share of this ring, about 1/3 (RD 97). From the fluxes at 20 cm and 6 cm, we computed a spectral index of -0.93 , which indicates that the synchrotron emission is predominant in these maps. There is a high star formation rate in the central part of NGC 1530, giving rise to radio continuum emission via synchrotron emission from supernova remnants. These supernova remnants give rise to most of the compact sources in the cm maps.

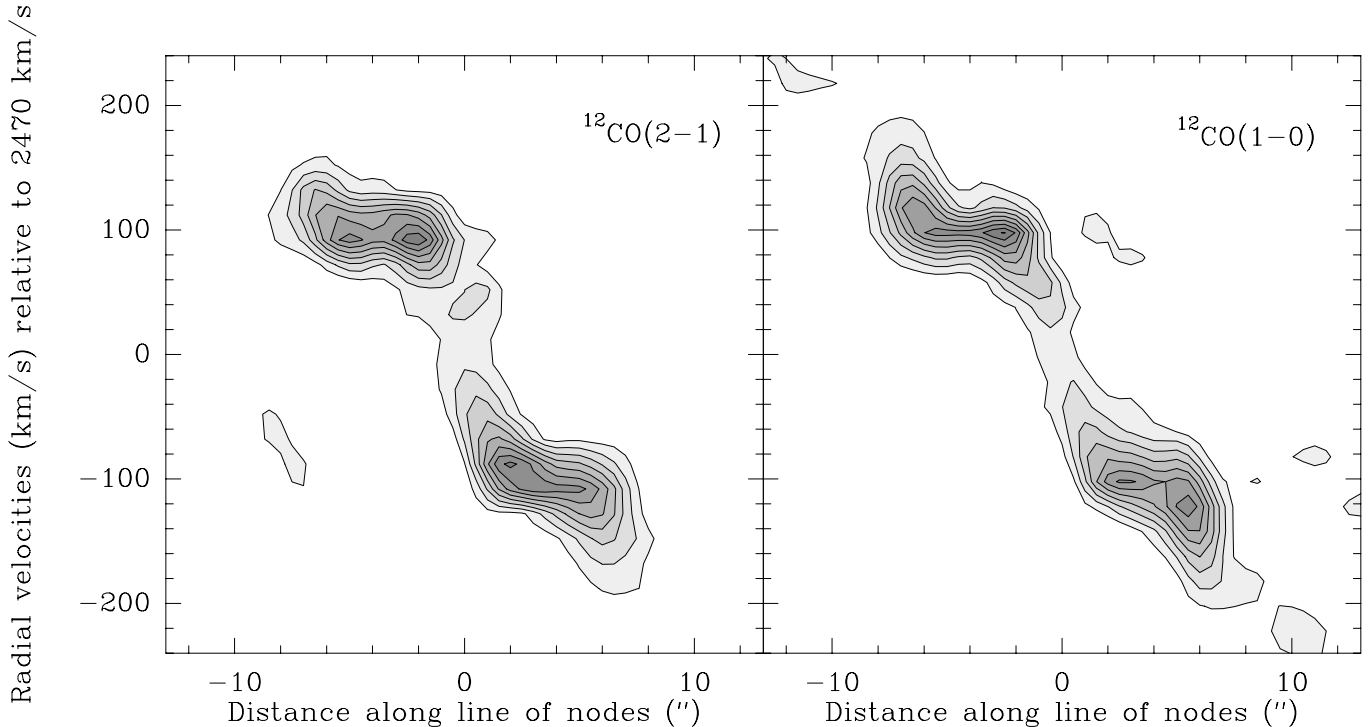


Fig. 4. Position velocity diagrams in $^{12}\text{CO}(2-1)$ (left, contour levels $0.03 \text{ Jy beam}^{-1}$) and $^{12}\text{CO}(1-0)$ (right, contour levels $0.015 \text{ Jy beam}^{-1}$). The horizontal coordinate is a distance offset (in arcsec) from the dynamical center along the line of nodes (p.a. 5°). The vertical coordinate is a radial velocity offset relative to 2470 km s^{-1} .

4. Discussion

4.1. Physical conditions of the gas

The previous maps reveal two main features for the molecular gas (also RD 97): *a*) Two intense arcs in both ^{12}CO lines and with little HCN; *b*) A nuclear ring or spiral with strong HCN and $^{13}\text{CO}(1-0)$. The radio continuum maps show a distribution similar to HCN, an intense ring and weak arcs.

To discuss these results more quantitatively, we chose five regions in the nuclear disk of NGC 1530, and calculated the various line ratios for these regions. Figure 1 shows these regions on the $^{12}\text{CO}(1-0)$ map. Table 2 gives their coordinates and the line ratios, along with the intensity of $^{12}\text{CO}(1-0)$ and fluxes from the cm maps convolved to a $2''.5$ gaussian for a better signal to noise ratio. We now relate the kinematics and the physical conditions of the gas in these regions.

Regions 2, 3 and 5 correspond to local maxima of $^{12}\text{CO}(1-0)$ and $^{12}\text{CO}(2-1)$ emission. Region 1 is a local maximum of $^{12}\text{CO}(2-1)$ and HCN($1-0$) while region 4 corresponds to a local minimum of $^{12}\text{CO}(1-0)$ and $^{12}\text{CO}(2-1)$. These regions are typical of the differing conditions in the nuclear disk. We have compared the location of these five regions with a CO($1-0$) velocity map from RD 97. Regions 1 and 2 correspond to a nearly circular rotation of the gas, as they are at the contact point between the

arcs and the nuclear ring. They are close to the dynamical center, at a radius of 0.7 kpc. Regions 3 and 4, at radii of 1.7 kpc, correspond to transition points in the kinematics, a transition between infall motions (in the CO arcs) and circular rotation (in the ring). Region 5 is further out in the southwest arc, at a 3 kpc radius. The motion of this region has an infall component of 70 km s^{-1} . This infall motion is associated with the density wave of the arc (RD 97).

The molecular ratios seem normal in the nuclear disk of NGC 1530. We compare the central kpc of NGC 1530 to the center of the spiral galaxy IC 342 which probably contains a weak bar (see Downes et al. 1992, Wright et al. 1993). IC 342 is one of the rare galaxies which has been observed in several different molecules with interferometers. IC 342 shows straight regular $^{12}\text{CO}(1-0)$ lanes (Wright et al. 1993, their Fig. 2b) that are curved near the nucleus, similarly to NGC 1530. The lanes emit in $^{13}\text{CO}(1-0)$ (Wright et al. 1993, their Fig. 2b) but not in HCN($1-0$) (Downes et al. 1992, their Fig. 1); in these two transitions one finds five 50 pc diameter clumps at the places where the lanes curve toward the nucleus. These clumps are not prominent in $^{12}\text{CO}(1-0)$. $R_{12/13}$ is 4.4 in these clumps and ≥ 20 in the CO lanes. Similarly, $R_{\text{CO}/\text{HCN}}$ is 7 in the clouds and ≥ 20 in the CO lanes. Therefore the results seem similar for both galaxies, with ratios $R_{12/13}$ and $R_{\text{CO}/\text{HCN}}$ lower near the nucleus ($r < 100 \text{ pc}$ for IC 342, $r < 700 \text{ pc}$ for NGC 1530). The places where the CO lanes

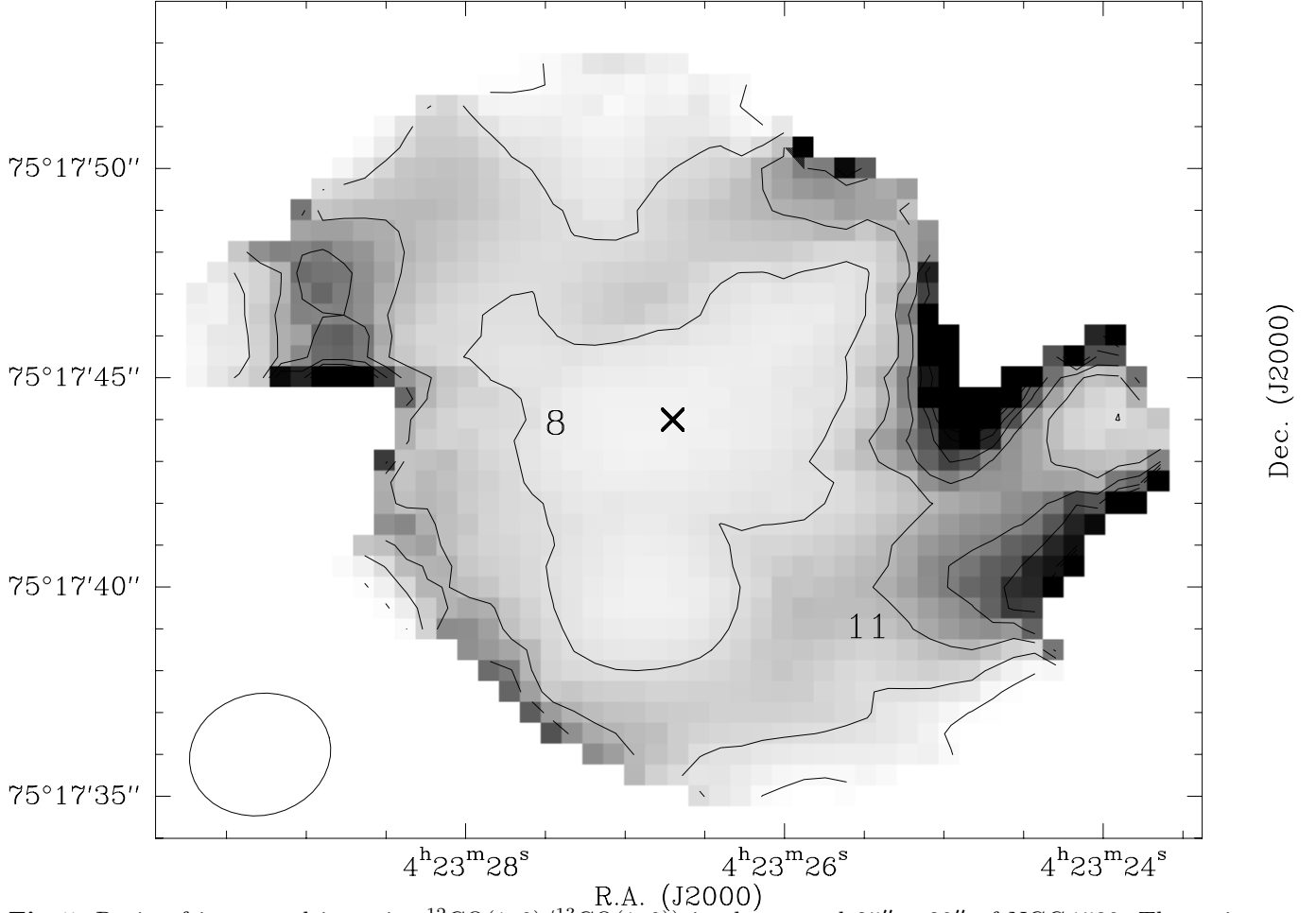


Fig. 5. Ratio of integrated intensity $^{12}\text{CO}(1-0)/^{13}\text{CO}(1-0)$ in the central $25'' \times 20''$ of NGC 1530. The ratio was calculated with a 2σ threshold for each transition. The greyscale runs from 4 to 20 (white to black). The contour levels are from 5 to 20 by 3. Labels indicate levels 8 and 11. The beam is indicated by an ellipse in the lower left corner. The **X** sign indicates the position of the dynamical center.

Table 2. Line ratios and cm fluxes in five regions of the center of NGC 1530.

| Region | R.A. ^a (s) | Dec. ^a ($''$) | $I(\text{CO})$ ^b (K km s $^{-1}$) | $R_{21/10}$ ^c | $R_{12/13}$ | $R_{\text{CO}/\text{HCN}}$ | $S_{20\text{cm}}$ ^d (mJy beam $^{-1}$) | $S_{6\text{cm}}$ (mJy beam $^{-1}$) | Spectral Index |
|--------|--------------------------|-------------------------------|--|--------------------------|-------------|----------------------------|---|---|----------------|
| 1 | 26.0 | 45.5 | 183 | 0.91 | 6.9 | 8.0 | 1.87 | 0.78 | -0.72 |
| 2 | 27.0 | 42.0 | 206 | 0.77 | 6.9 | 13.0 | 1.77 | 0.63 | -0.85 |
| 3 | 28.0 | 49.0 | 273 | 0.67 | 9.9 | 28.8 | 0.78 | 0.30 | -0.79 |
| 4 | 25.5 | 38.0 | 104 | 0.82 | 8.9 | 14.1 | 1.09 | 0.51 | -0.63 |
| 5 | 24.7 | 40.5 | 168 | 0.76 | 14.9 | > 25.6 | 0.52 | 0.12 | -1.22 |

^a Coordinates (J2000): $04^{\text{h}}23^{\text{m}}; +75^{\circ}17'$

^b $^{12}\text{CO}(1-0)$ integrated intensity

^c Line ratios $^{12}\text{CO}(2-1)/^{12}\text{CO}(1-0)$, $^{12}\text{CO}(1-0)/^{13}\text{CO}(1-0)$ and $^{12}\text{CO}(1-0)/\text{HCN}(1-0)$

^d 20 cm, 6 cm fluxes in $2''.5$ diameter lobes

become a nuclear ring or spiral show large emissivity in $^{13}\text{CO}(1-0)$ and $\text{HCN}(1-0)$, which can be interpreted as the sign of a high concentration of dense gas (see, e.g., Downes et al. 1992, Mauersberger & Henkel 1993).

We supposed that the ^{12}CO and ^{13}CO transitions are emitted by the same masses of gas. Therefore we

could run escape probability models, to reproduce the observed line ratios of CO. We assumed the following values for the abundance ratios : $[^{12}\text{CO}]/[\text{H}_2] = 10^{-4}$ and $[^{12}\text{CO}]/[^{13}\text{CO}] = 60$. We assumed a velocity gradient of $1\text{ km s}^{-1}\text{ pc}^{-1}$. Table 3 displays the results of the best fitting model. We deduced from this model the expected H_2

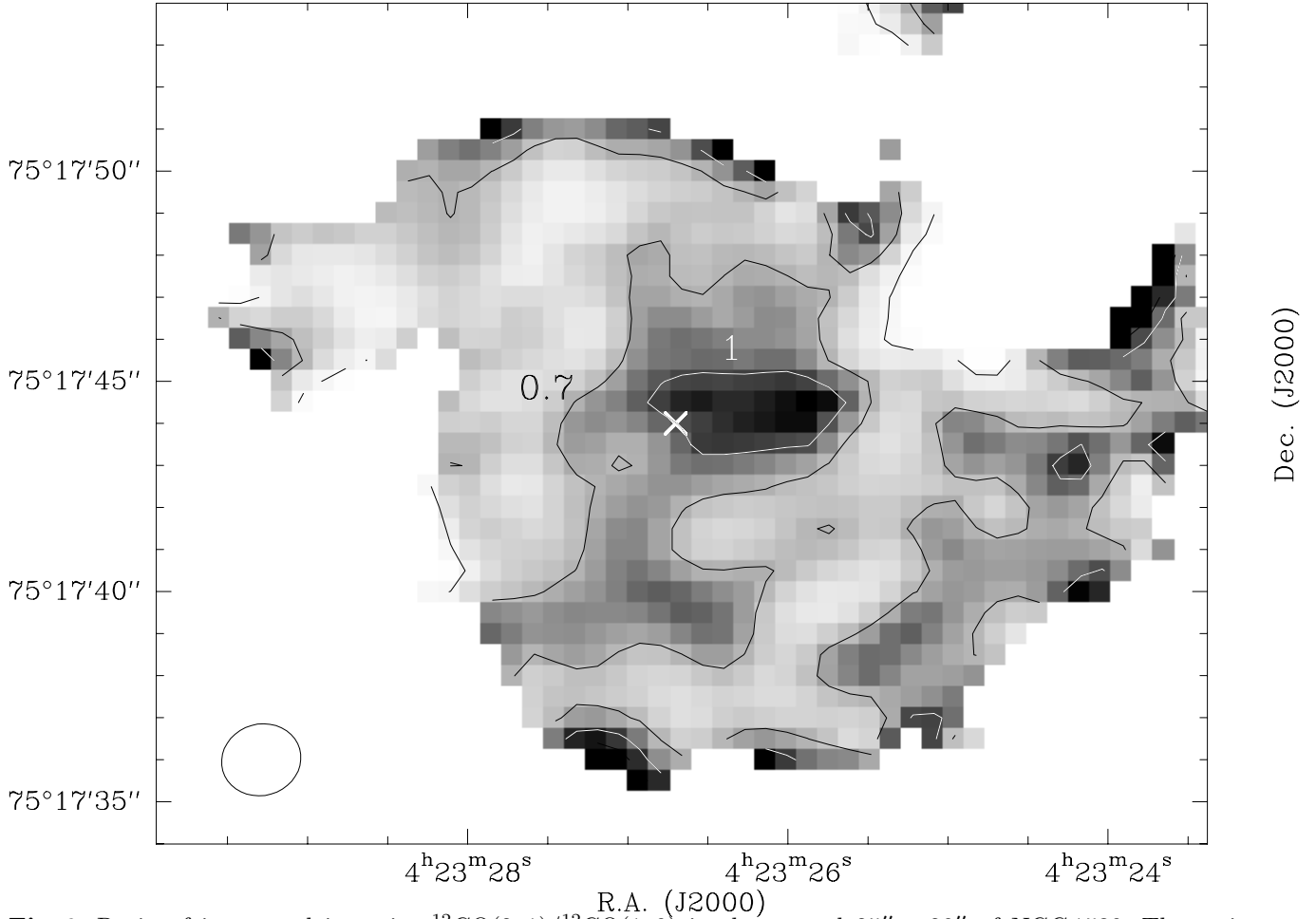


Fig. 6. Ratio of integrated intensity $^{12}\text{CO}(2-1)/^{12}\text{CO}(1-0)$ in the central $25'' \times 20''$ of NGC 1530. The ratio was calculated with a 3σ threshold for each transition. The greyscale runs from 0.3 to 1.2 (white to black). The contour levels are from 0.4 to 1.3 by 0.3. Labels indicate levels 0.7 and 1.0 (in white contour). The beam is indicated by an ellipse in the lower left corner. The **X** sign indicates the position of the dynamical center.

density and kinetic temperature of the emitting gas for each region. Then we could derive the theoretical brightness temperature and obtain a filling factor by computing the ratio $T_b^{\text{obs}}/T_b^{\text{th}}$. We computed also for each one of these 5 regions the CO to H_2 conversion factor, using the formula $M(\text{H}_2)/L_{\text{CO}} = 2.1 n(\text{H}_2)^{1/2}/T_b(\text{CO}(1-0))$, in units of $M_{\odot} (\text{K km s}^{-1} \text{pc}^2)^{-1}$ (Radford et al. 1991). This formula is valid for an ensemble of virialized molecular clouds, which is the case here.

The derived kinetic temperatures are standard values for the molecular gas, between 20 and 90 K. This kinetic temperature is weakly constrained by the escape probability calculations, and the error bars of the measured ratios do not allow a precise derivation. The H_2 density is more tightly constrained. The gas density is greater near the center ($\gtrsim 5 \times 10^2 \text{ cm}^{-3}$) than in the arms (2 to 3×10^2). Region 4 has a greater density than the equivalent region 3. Regions with greater density (1, 2, 4) show a stronger HCN emission than the ones with a lower density, confirming

the association of HCN emission with dense gas (Mauersberger & Henkel 1993). The derived filling factors are loosely constrained, as are the theoretical CO(1-0) brightness temperatures, depending on the kinetic temperatures. The average value is $\langle f \rangle \simeq 0.15$. These low values reveal the clumpy nature of the molecular gas, contained in many small molecular clouds, unresolved with the $\simeq 500 \text{ pc}$ beam of the interferometer. The derived values for the conversion factor have an average of $\langle M(\text{H}_2)/L_{\text{CO}} \rangle \simeq 1.4 M_{\odot} (\text{K km s}^{-1} \text{pc}^2)^{-1}$. This is lower than the average value for the giant molecular clouds of our own galaxy ($M(\text{H}_2)/L_{\text{CO}} \simeq 4.8 M_{\odot} (\text{K km s}^{-1} \text{pc}^2)^{-1}$, Sage & Isbell 1991). Region 5 has a conversion factor significantly lower than the others, possibly due to different excitation conditions for the molecular transitions.

We found in the central kiloparsec of NGC 1530 a $M(\text{H}_2)/L_{\text{CO}}$ ratio about three times lower than the standard galactic value of Sage & Isbell (1991). It is unlikely that this conversion factor is universal. For the inner

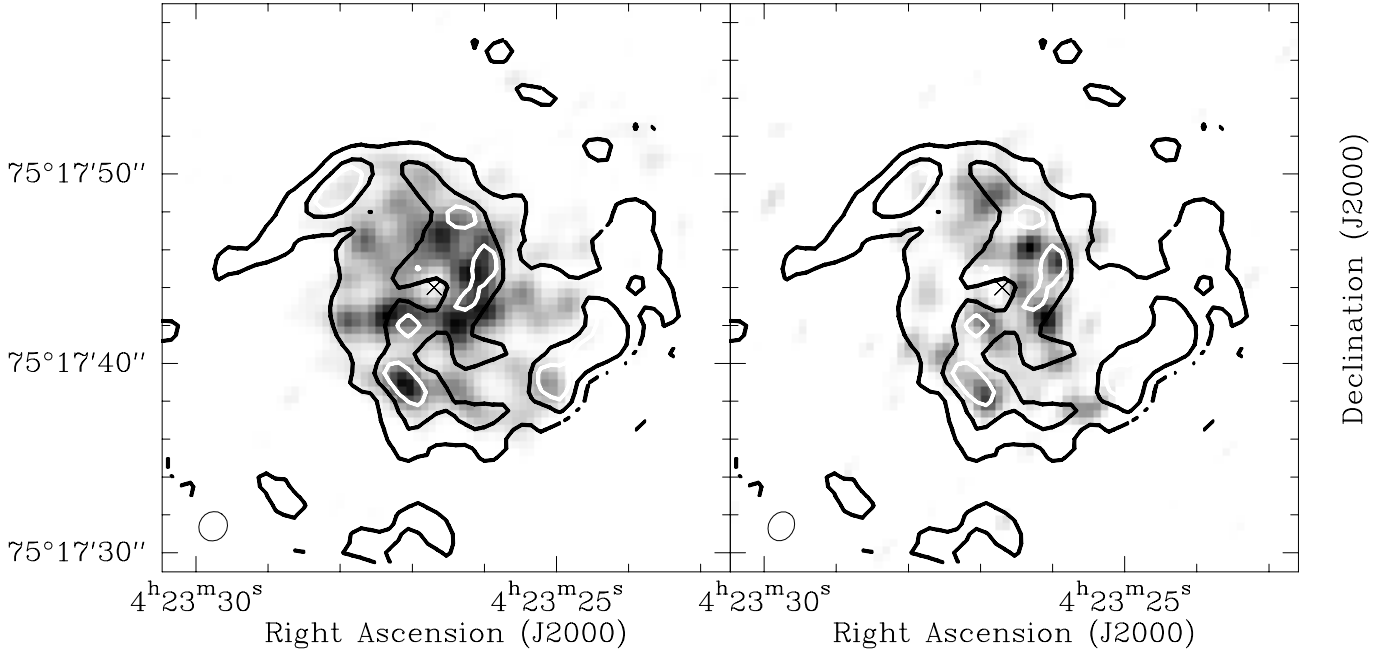


Fig. 7. *a)* Left: $^{12}\text{CO}(2-1)$ superposed on a grey scale map of the radio continuum at $\lambda = 20$ cm. The grey scale runs from $0.18 \simeq 2\sigma$ to $1.0 \text{ mJy beam}^{-1}$. *b)* Right: $^{12}\text{CO}(2-1)$ superposed on a grey scale map of the radio continuum at $\lambda = 6$ cm. The grey scale runs from $0.10 \simeq 2\sigma$ to $0.42 \text{ mJy beam}^{-1}$. The contours show the 6, 14 (black) and 18 mJy beam^{-1} levels of the integrated intensity of $^{12}\text{CO}(2-1)$. The cm-radio continuum lobes are indicated by ellipses in the lower left corners. The dynamical center is indicated by a **X** sign. The cm-radio continuum maps are partially presented in Saikia et al. (1994), and were made kindly available by Dr. A. Pedlar.

Table 3. Results from an escape probability analysis for the regions of Table 2.

| Region | $n(\text{H}_2)^a$ ($10^2 \times \text{cm}^{-3}$) | T_{kin}^b (K) | $T_{\text{b}}^{\text{obs } c}$ (K) | $T_{\text{b}}^{\text{th } d}$ (K) | f^e | $M(\text{H}_2)/L_{\text{CO}}^f$ |
|--------|---|---------------------------|---------------------------------------|--------------------------------------|-------|---------------------------------|
| 1 | 8.2 | 51 | 2.7 | 32.3 | 0.08 | 1.2 |
| 2 | 4.7 | 20 | 2.6 | 12.8 | 0.2 | 2.3 |
| 3 | 3.1 | 18 | 3.2 | 9.8 | 0.3 | 2.0 |
| 4 | 4.5 | 40 | 1.5 | 20.6 | 0.07 | 1.1 |
| 5 | 2.1 | 85 | 2.1 | 16 | 0.13 | 0.35 |

a H_2 density

b Model kinetic temperature

c Observed $^{12}\text{CO}(1-0)$ brightness temperature

d Model $^{12}\text{CO}(1-0)$ brightness temperature

e Area filling factor of molecular clouds

f Conversion factor (in $M_{\odot} (\text{K km s}^{-1} \text{pc}^2)^{-1}$) computed from $M(\text{H}_2)/L_{\text{CO}} = 2.1 n(\text{H}_2)^{1/2}/T_{\text{b}}(\text{CO}(1-0))$

14 kpc diameter region of NGC 891, Guélin et al. (1993) found a ratio 3 times lower than the standard galactic value. For the innermost 11 kpc of M51, Guélin et al. (1995) found a ratio 4 times lower than the standard galactic value. Our results are similar to the results found by Guélin et al. (1993, 1995). In the inner 1200 pc of the Milky Way, Dahmen et al. (1998) found a factor of 10 discrepancy relative to the standard Galactic value. We do not find comparable results in the inner kiloparsec of NGC 1530.

4.2. Star formation and dense gas

Helou et al. (1985) found a proportionality between the far infrared flux and the 20 cm flux for disks of spiral galaxies. This proportionality indicates that the *global* star formation rate and the *global* 20 cm flux are linearly correlated. We assumed a linear correlation between the *local* star formation rate and the *local* 20 cm flux density. Thus for each of the 5 regions we computed its local star formation rate SFR^{loc} in a $2''.5$ beam by the following formula, with $S_{20\text{cm}}^{\text{tot}} = 80 \text{ mJy}$ (total 20 cm flux from NGC 1530,

Table 4. Star formation rates and masses of dense gas ($n(\text{H}_2) \simeq 10^4 \text{ cm}^{-3}$) in the five regions of Table 2.

| Region | $SFR^{\text{loc } a}$ ($10^{-2} M_{\odot} \text{ an}^{-1}$) | $M_{\text{HCN}}(\text{H}_2)^b$ ($10^7 M_{\odot}$) |
|--------|--|--|
| 1 | 6 | 16 |
| 2 | 5 | 11 |
| 3 | 2 | 4 |
| 4 | 3 | 8 |
| 5 | 1 | 5 |

a Local star formation rates from 20 cm flux in a $2''.5$ beam

b Dense gas masses from HCN integrated fluxes in a $3''.5$ beam from $M_{\text{HCN}}(\text{H}_2)/L_{\text{HCN}} \simeq 20 M_{\odot} (\text{K km s}^{-1} \text{ pc}^2)^{-1}$

from Wunderlich et al. 1987, Condon et al. 1996) and $SFR^{\text{tot}} = 2.4 M_{\odot} \text{ yr}^{-1}$

$$SFR^{\text{loc}} = \frac{S_{20\text{cm}}^{\text{loc}}}{S_{20\text{cm}}^{\text{tot}}} SFR^{\text{tot}}$$

To compare with the dense gas distribution, we calculated the amount of H_2 gas in dense phase present in each one of these five regions. We used for that the relation existing between the mass of dense gas and the velocity integrated HCN intensity. This relation is derived from HCN radiative transfer solutions (Solomon et al. 1992). It can be written as $M_{\text{HCN}}(\text{H}_2)/L_{\text{HCN}} \simeq 20 M_{\odot} (\text{K km s}^{-1} \text{ pc}^2)^{-1}$, where $M_{\text{HCN}}(\text{H}_2)$ is the mass of H_2 at a density $\simeq 10^4 \text{ cm}^{-3}$ as traced by HCN. From the HCN fluxes of Fig. 1 and this relation, we computed the molecular gas masses of Table 4. The comparison of SFR^{loc} and $M_{\text{HCN}}(\text{H}_2)$ show that the star formation rate seems correlated with the amount of available dense gas. The region 4 shows a higher SFR^{loc} and a higher amount of dense gas than regions 3 and 5, even though region 4 is included in an arc, like the other two regions. Region 5 shows a very low level of star formation, consistent with its cm wavelength spectral index, -1.2 (see Table 2), which indicates the absence of thermal component in the cm emission.

5. Conclusion

We studied the inner molecular disk of the barred spiral galaxy NGC 1530 by means of millimeter interferometry. The main conclusions of this paper are :

— The $^{12}\text{CO}(2-1)$ intensity map obtained with a $1''.6$ resolution is very similar to the $^{12}\text{CO}(1-0)$ distribution, with a nuclear ring, and around it, two bright curved arcs.

— The $^{13}\text{CO}(1-0)$ intensity map synthesized with a $3''.1$ beam is rather similar to the $^{12}\text{CO}(1-0)$ map, with weaker curved arcs.

— The average ratios are $R_{12/13} = 9$ and $R_{21/10} = 0.7$, comparable to other spiral galaxies. $R_{12/13}$ shows a general decrease from the central ring ($R_{12/13} \simeq 6-8$) to the curved arcs ($R_{12/13} \simeq 11-15$). $R_{21/10}$ shows no such

systematic trend. The ratio is highest ($\simeq 1.2$) in a region close to the dynamical center.

— The VLA cm maps show a ring very similar to the ^{12}CO ring, but little or no emission in the curved arcs.

— An escape probability analysis reproduces well the line ratios in five regions of the disk. We could derive the kinetic temperature and the density of the gas, together with filling factor. The gas density seems higher in the nuclear ring than in the curved arcs, except for an isolated region in the south-western arc.

— The conversion factor deduced from this model is $M(\text{H}_2)/L_{\text{CO}} \simeq 1.4 M_{\odot} (\text{K km s}^{-1} \text{ pc}^2)^{-1}$, three times lower than the standard galactic value of $4.8 M_{\odot} (\text{K km s}^{-1} \text{ pc}^2)^{-1}$.

— The star formation rate as calculated from the 20 cm flux and the mass of dense gas deduced from the HCN flux are spatially correlated.

Acknowledgements. We thank the technical staff of the IRAM interferometer for the remarkable job they do. We thank Dr. Alan Pedlar for making available the VLA data. We thank the referee Dr. Vogel for helpful comments.

References

- Athanassoula E., 1992, MNRAS 259, 345.
 Braine J., Combes F., Casoli F., Dupraz C., Gerin M., Klein U., Wielebinski R., Brouillet N., 1993, A & A S 97, 887
 Condon J.J., Helou G., Sanders D.B., Soifer B.T., 1996, ApJS 103, 81
 Dahmen G., Huttemeister S., Wilson T.L., Mauersberger R., 1998, A & A 331, 959
 Downes D., Radford S.J.E., Guilloteau S., Guélin M., Greve A., Morris D., 1992, A & A 262, 424
 Downes D., Reynaud D., Solomon P.M., Radford S.J.E., 1996, ApJ 461, 186
 Eckart A., Downes D., Genzel R., Harris A.I., Jaffe D.T., Wild W., 1990, ApJ 348, 434
 Friedli D., Benz W., 1993, A & A 268, 65
 Greve A., Reynaud D., Downes D., 1999, A & A submitted.
 Guélin M., Zylka R., Mezger P.G., Haslam C.G.T., Kreysa E., Lemke R., Sievers A.W., 1993, A & A 279, L37
 Guélin M., Zylka R., Mezger P.G., Haslam C.G.T., Kreysa E., 1995, A & A 298, L29
 Guilloteau S., Delannoy J., Downes D., Greve A., Guélin M., Lucas R., Morris D., Radford S., Wink J., Cernicharo J., Forveille T., Garcia-Burillo S., Neri R., Blondel J., Perregouard A., Plathner D., Torres M., 1992, A & A 262, 624
 Helou G., Soifer B.T., Rowan-Robinson M., 1985, ApJ 298, L7
 Knapp G.R., Phillips T.G., Huggins P.J., Leighton R.B., Wannier P.G., 1980, ApJ 240, 60
 Loiseau, N., Nakai, N., Sofue, Y., Wielebinski, R., Reuter, H.-P., Klein, U., 1990, A & A 228, 331
 Mauersberger R., Henkel C., 1993, ARA & A 6, 69
 Piner B.G., Stone J.M., Teuben P.J., 1995, ApJ 449, 508
 Plambeck R.L., Williams D.R.W., 1979, ApJ 227, L43
 Radford S.J.E., Solomon P.M., Downes D., 1991, ApJ 368, L15
 Regan M.W., Vogel S.N., Teuben P.J., 1995, ApJ 449, 576

- Regan M.W., Teuben P.J., Vogel S.N., van der Hulst T., 1996,
AJ 112, 2549
- Reynaud D., Downes D., 1997, A & A 319, 737
- Reynaud D., Downes D., 1998, A & A 337, 671
- Sage L.J., Isbell D.W., 1991, A & A 247, 320
- Saikia D.J., Pedlar A., Unger S.W., Axon D.J., 1994, MNRAS
270, 46
- Sakamoto S., Handa T., Sofue Y., Honma M., Sorai K., 1997,
ApJ 475, 134
- Solomon P.M., Downes D., Radford S.J.E., 1992, ApJ 387, L55
- Wright M.C.H., Ishizuki S., Turner J.L., Ho P.T.P., Lo K.Y.,
1993, ApJ 406, 470
- Wunderlich E., Klein U., Wielebinski R., 1987, A&AS 69, 487